MODELLING *M(3000)F2* AT AN AFRICAN EQUATORIAL LOCATION FOR BETTER IRI-MODEL PREDICTION

J. O. Adeniyi[1,2], B. O. Adebesin[1,2,3,*], P. A. Afolabi[4], S. O. Ikubanni[1, 2], S. J. Adebiyi[1, 2].

[1]*Climate Action SDG 13 Group, Landmark University, Omu-Aran, Nigeria.*

[2]*Department of Physical Sciences, Landmark University, P.M.B 1001, Omu-Aran, Nigeria.*

[3]*Landmark University Centre for Research, Innovation and Discoveries (LUCRID), Nigeria.*

[4]*Department Physics, College of Education, Oro, Kwara State, Nigeria.*

*Corresponding Author: f_adebesin@yahoo.co.uk; adebesin.olufemi@lmu.edu.ng. (B. O. Adebesin)

Key points:

- The seasonal dependence of *M(3000)F2 at Korhogo* on solar activity is more pronounced at nighttime in comparison to daytime observations.
- The empirical constructed model allows the prediction of diurnal, seasonal and solar cycle variation of the *M(3000)F2* parameter.
- The 'constructed model' ($M(3000)F2_{CM}$) performed well when tested at different solar activity conditions.

Abstract:

The F2-layer propagation factor *M(3000)F2* is important to ionospheric studies owning to its use in HF radio communication/ionospheric modelling. This study focused on reducing the shortcomings in the use of *M(3000)F2* IRI-model for obtaining *hmF2*, especially in the African equatorial region, by obtaining an empirical 'constructed model' ($M(3000)F2_{CM}$) using the Korhogo (geomag. lat. 1.26°S, long. 67.38°E, dip.-0.67^{0}S) data ($M(3000)F2_{KOR}$). The data spans 8 years (1993-2000) under magnetically quiet conditions (*Ap*< 20nT). The Regression method technique was used in obtaining the $M(3000)F2_{CM}$. The $M(3000)F2_{KOR}$ results revealed that low solar activity (LSA) years have predominantly higher magnitudes than high solar activities (HSA) for all seasons, revealing solar activity dependence. The regression coefficient (R^2) for the $M(3000)F2_{KOR}$ versus *F10.7* relationship was stronger during the solstices. The associated diurnal equations obtained for all seasons from the regression plot of the $M(3000)F2_{KOR}$-*F10.7* relationship were used to obtained the constructed model equation given by $M(3000)F2_{CM}(m)_i = a_i(m) * (F10.7) + b_i$, which allows the prediction of diurnal, seasonal and solar cycle variation of the *M(3000)F2* parameter. $M(3000)F2_{CM}$ predicted well when tested at different solar activities. Generally, $M(3000)F2_{CM}$ performed reasonably well in comparison with the IRI model ($M(3000)F2_{IRI}$) when validated with Ouagadougou (lat. 0.59°S, long. 71.46°E) observed data - $M(3000)F2_{OUA}$. The %deviation of $M(3000)F2_{CM}$ versus $M(3000)F2_{OUA}$ during HSA and LSA ranges from -10.8- 5.3/-7.6 - 15.8 for solstices/equinoxes; whereas %deviation of $M(3000)F2_{IRI}$ versus $M(3000)F2_{OUA}$ spans -15.5-9.2 and -9.7-17.7 in similar order of seasons. These results suggest that the new model has a measure of potential for its use in the equatorial region.

Keywords: *Ionosphere; Ionospheric propagation factor M(3000)F2; equator; IRI-model; African sector.*

1. Introduction:

1.1. Background to the study

Radio communication systems designers and professionals require sufficient information and facts on the structure and characteristics of radio propagation in the ionosphere, in planning for working and acceptable frequencies. The ionosphere on the other hand has a complex structure with numerous variables and irregularities that can affect radio communication propagations. Thus, High frequency (HF) radio communication relies on the behaviors of the ionosphere. Consequently, there is need for consistent and reliable estimate of several ionospheric parameters for adequate planning and navigational purposes [Adeniyi et al., 2021]. The electron density of the ionosphere on which the working frequency depends varies with different components, including the time of the day, season of the year, phase of the solar cycle, magnetic activity condition, as well as the latitude of the region of interest [Obrou

et al., 2003; Adebesin et al., 2018a]. Coupled with these irregularities are also the short-duration constraints posed by atmospheric radio noise, solar-flare and radio fadeouts of the African sector [Falayi et al., 2018; Adebesin et al., 2019]. However, satellite communication which is almost free from these shortcomings observed in radio communications is expensive due to high installation cost. Consequently, since the finance is not always readily available for installing artificial satellite, the need to maximize skywave propagation becomes expedient. HF radio communication stands to be the inexpensive option available for long distance radio broadcasting, and the ionospheric propagation factor *M(3000)F2* is a parameter needed to achieve this goal.

The *M(3000)F2* is the highest frequency at which a radio wave can be obtained over a distance of 3000 km after reflection in the ionosphere, and it is defined as the ratio of the maximum usable frequency (MUF) at a distance of 3000km to the F2 layer critical frequency (foF2) given by the relation in equation (1).

$$M(3000)F2 = \frac{MUF}{foF2} \quad (1)$$

The *M(3000)F2* is very important because of its use in the prediction of the height of the F2-layer peak electron density (*hmF2*), as well as for frequency planning in HF (3MHz – 30MHz) radio communication and ionospheric modelling [Oyeyemi et al., 2007]. According to Hoque and Jakowsi (2012), while Shimazaki (1955) established an inverse relationship between *hmF2* and *M(3000)F2*; Bradley and Dudeney (1973) and Bilitza et al. (1979) observed better relationship between the two parameters after introducing the *foF2/foE* ratio, geomagnetic latitude, and sunspot number alongside *M(3000)F2* in the determination of *hmF2* magnitude. *foF2* and *foE* being the respective critical frequencies in the F2 and E ionospheric layers.

Various techniques have been employed in the modelling of *M(3000)F2*. Some of these include the Neural Network (NN) technique [Oyeyemi et al., 2007; Bilitza et al., 2011], the Empirical Orthogonal Function technique [Liu et al., 2008; Zhang et al., 2010], and the Regression method [Tukhashvili et al., 2003]. Adeniyi et al. [2003] using Ouagadougou (lat. 12.4^0N, long. 1.5^0W) ionosonde data in the African sector had shown that the post-sunset *hmF2* peak are reproduceable if measured *M(3000)F2* are used instead of the IRI-CCIR *M(3000)F2* model. Obrou et al. [2003] studied the response of equatorial F2-peak parameters in the IRI-map. They reported that while the general diurnal variation of *M(3000)F2* is well indicated by the IRI-CCIR model, the pattern obtained with the *M(3000)F2* model is not sufficient to duplicate small-scale spatial and temporal characteristics, including the evening-time sharp drop in *M(3000)F2* that parallels the post-sunset *hmF2* peak. With the injection of the measured *M(3000)F2* into the IRI-model, the map reproduces the sharp post-sunset F2-layer peak feature well. This result obtained by Obrou et al. [2003] was noteworthy, as the inability to accurately predict the evening-time peak has frequently been noted as an essential limitation of the IRI-model, especially in the African sector. Some other shortcomings of the *M(3000)F2* IRI-model include (a) its inability to reproduce the detailed diurnal structure of *M(3000)F2* [Adeniyi et al. 2003], and (b) underestimating /overestimating the observed values of *M(3000)F2* [Zhang et al., 2010; Oyekola, 2010). These limitations in the *M(3000)F2* IRI-model was suggested by Obrou et al. [2003] to have emanated from the small number of Fourier terms employed in describing the diurnal variation. In another sense, it may be argued that the challenges are manifesting in the African equatorial region because the IRI-model was originally developed with data from the American sector including Jicamarca, Peru and Arecibo, Puerto Rico [Bilitza et al., 1979] owning to lack of adequate database in the African sector.

The neural network technique (NN) for the global modelling of *M(3000)F2* was employed by Oyeyemi et al. [2007] with data covering 1964–1986 from 51 stations across all latitudes, and geomagnetic activity conditions taken into consideration. The authors obtained results that compares well with the IRI-model, and justifies the use of NN as a good alternative (owning to low error differences) for treating *M(3000)F2* on a global scale. Ehinlafa et al. [2010] - during low-solar activity; and Oyekola [2010] – during magnetically quiet condition of low and high solar

conditions; also reported variance in the post-sunset *hmF2* peak pattern obtained from the measured *M(3000)F2* and that of the IRI-model at Ouagadougou for different study periods.

1.2. Current study

This study is therefore set at reducing the shortcomings encountered in the use of *M(3000)F2* IRI-model (which is the widely adopted ionospheric climatological model for obtaining *hmF2*. It is believed that if the modelled *M(3000)F2* is gotten right, the prediction of the post-sunset peak of the maximum height of reflection in the F2-layer (*hmF2)* inferred from *M(3000)F2* will be left with little inaccuracies. *hmF2* is important for the study of ionospheric electrodynamics [Adebesin et al., 2018b; Adebiyi et al., 2020], for inferring the vertical plasma drift [Adebesin and Adeniyi, 2018], as well as for obtaining neutral meridional winds [Liu et al., 2003] among other purposes. Besides, it is believed that the model to be presented in this work will serve as an improvement to *IRI-M(3000)F2* predicted values, and will improve frequency planning in HF radio communication in the African sector, most especially the equatorial region. Consequently, the present work aims at (i) investigating the *M(3000)F2* morphology at an equatorial station in the African sector; (ii) establishing a regression linear relationship between *M(3000)F2* and the solar flux index, *F10.7*; (iii) obtaining a model equation for *M(3000)F2*; and (iv) validating the obtained model with data from another equatorial station, and (v) comparing the obtained model with that of the IRI-2012 model. Consequently, the data used and method of analysis was presented in section 2. Section 3 highlights the results and discussion, with the concluding remarks depicted in Section 4.

2. Data and method

Four types of data were employed. This are the measured *M(3000)F2* data (2 sources), the solar flux index (*F10.7*) data, and the IRI-2012 (ITU-R) model *M(3000)F2* data. The first set of data are the daily hourly values of measured *M(3000)F2*, and was obtained from ionograms recorded using the Ionospheric Prediction Service IPS-42 sounder located at Korhogo (geographic lat. 9.51°N, long. 354.40°E, dip lat. - 0.67^0S; geomagnetic lat. 1.26°S, long. 67.38°E) in the equatorial dip of the African sector. The data used spans 8 years covering January 1993 to December 2000 for magnetically quiet conditions (*Ap* < 20 nT) which was manually validated. The daily hourly values of the *M(3000)F2* parameter were later used to compute the hourly monthly average values for the diurnal and seasonal classifications. The seasons were categorized into March equinox (February, March, April), June solstice (May, June, July) September equinox (August, September, October), and December solstice (November, December, January). Second is the data of *F10.7*, which reveals the extent of the noise level of the Sun at 10.7 cm wavelength in the Earth's orbit, and a proxy parameter for measuring solar input. The *F10.7* data was made available by the Natural Resources Canada online website at http://www.spaceweather.ca/solarflux/sx-5-en.php.

The third dataset is for the *M(3000)F2* obtained from the IPS-42 sounder located at Ouagadougou (geographic lat. 12.42°N, long. 358.60°E, dip lat. – 5.9^0N; geomagnetic lat. 0.59°S, long. 71.46°E), another dip equatorial latitude station in the African sector. Ouagadougou data is used for the validation of the model to be developed from the Korhogo *M(3000)F2* data. Consequently, the data to be used for Ouagadougou are those of 1991 and 1995, representing the high- (*F10.7 = 208.1 sfu*) and low-solar (*F10.7 = 77.2 sfu*) activities respectively. Both the Korhogo and Ouagadougou data can be accessed through http://eprints.lmu.edu.ng/2918/. Additional information could be obtained from the Ionosonde Network Advisory Group (INAG), website on http://www.ips.gov.au/IPSHosted/INAG/web-73/index.html. INAG is a Working Group 1 of the International Radio Consultative Committee (URSI), with the responsibility of preserving the global ionospheric climate record, amongst other functions. The website is a consolidated database of worldwide values of ionospheric *M(3000)F2* and *foF2*. The data had been manually checked and corrected where necessary.

The fourth data used was that of the IRI-2012 (ITU-R) *M(3000)F2* model/predicted data. This was obtained from the web address https://ccmc.gsfc.nasa.gov/modelweb/models/iri2012_vitmo.php. The IRI-2012 model was used

to compare the 'constructed model' to be obtained using Korhogo *M(3000)F2* data. The International Telecommunication Union – Radio-communication sector (ITU-R) plays a vital role in the global management of radio spectrum and satellite orbits. For clarity, we have the following representations from this point forward:

a. $M(3000)F2_{KOR.}$ is the Korhogo *M(3000)F2* data
b. $M(3000)F2_{CM}$ is the newly empirical 'constructed model' using the Korhogo *M(3000)F2* data
c. $M(3000)F2_{IRI}$ depicts the IRI-2012 (ITU-R) predicted model.
d. $M(3000)F2_{OUA.}$ highlights the observed *M(3000)F2* data from Ouagadougou for validation purpose

It is worth mentioning that the years 1993, 1994, 1995, 1996, 1997, 1998, 1999, and 2000 $M(3000)F2_{KOR.}$ data used have corresponding annual solar flux index values of 109.7sfu, 85.7sfu, 77.2sfu, 72.0sfu, 80.7sfu, 118.7sfu, 153.4sfu, and 181.0 sfu respectively. This implies that the data covers the descending phase of solar cycle 22 (1993 -1996) and the ascending phase of solar cycle 23 (1996 – 2000). Further, 1994, 1995, 1996 and 1997 are low solar activity years, 1993 and 1998 being moderate solar activity years, while 1999 and 2000 are high solar activity conditions. The following arithmetic developments were also carried out on the $M(3000)F2_{KOR.}$ data

a. Monthly average hourly value is the arithmetic daily hourly mean value for a month
b. Annual average hourly value is the arithmetic hourly monthly mean value of months constituting a particular year (as in Figure 1).
c. Seasonal average hourly value is the arithmetic hourly monthly mean value of months constituting a season for the entire years considered (e.g. as in Figure 3). For instance the value at 12LT in March equinox is the arithmetic average of all data collected across the entire years for months constituting March equinox.

For this work, the Regression method technique similar to that used by Tukhashvili et al. [2003] was employed. The method is such that $M(3000)F2_{KOR}$ in a fixed point of a particular month depends on the solar activity and the Sun's zenith angle (a function of the local time). Hence, it is possible to establish a relationship between $M(3000)F2_{KOR}$ and *F10.7*. The procedures involved in the Regression method technique involves (i) performing a general trend observation on the data of $M(3000)F2_{KOR}$ versus *F10.7,* (ii) determining the regression coefficients (R^2), 'a' and 'b' between the two parameters using the least-square method. The least square lines were fitted using the monthly averages of $M(3000)F2_{KOR}$ as the dependent variable and *F10.7* as the independent variable. 'a' is the slope, and 'b' is the intercept, (iii) computing the R^2 values, and observing its diurnal characteristics, (iv) establishing the suitable model. Thereafter, the overall performance of the 'constructed model' $M(3000)F2_{CM}$ was validated with observed data from Ouagadougou $M(3000)F2_{OUA}$. Finally, the percentage deviation between $M(3000)F2_{CM}$ and $M(3000)F2_{OUA}$ during periods of solar minimum and maximum for the equinoxes and solstices were presented. Generally, the plots were presented from 06LT to 05LT separating the daytime (06LT -18LT) and nighttime (18LT – 05LT) observations. The observations were further buttressed in terms of the differences between the observed data from Ouagadougou and $M(3000)F2_{CM}$ (as well as the one between $M(3000)F2_{OUA}$ and $M(3000)F2_{IRI}$) using the statistical root mean square deviation (RMS_{dev}) tool. The $RMS_{dev,}$ which is a measure of the difference between two similar parameters is defined mathematically in the present context as:

$$RMS_{dev} = \sqrt{\frac{\sum_{i=1}^{n}(M(3000)F2_{OUA} - M(3000)F2_{CM})^2}{n}} \quad (2a)$$

and

$$RMS_{dev} = \sqrt{\frac{\sum_{i=1}^{n}(M(3000)F2_{OUA} - M(3000)F2_{IRI})^2}{n}} \quad (2b)$$

The lower the value between the two parameters, the better the relationship between them or the closer their deviation from one another (i.e. lower value presents better performance). n is the number of points/observations considered.

3. Results and Discussion:

3.1 Seasonal trend in M(3000)F2$_{KOR}$.

Figure 1(a) highlights the seasonal average hourly pattern of *M(3000)F2* at Korhogo (*M(3000)F2$_{KOR}$*) spanning 1993 through 2000. Generally, two major sharp crests were observed. First was the one at daytime hour of 07LT and the second was towards the nighttime period (04 -05LT). Sharp decrease was noticeable around 07LT till 11LT across all years and seasons irrespective of solar activity conditions. A little saturation in the magnitudes was however noted between 11LT and 16LT for all seasons (except June solstice) that eventually creates a well pronounced trough in the daytime observation. The nighttime observation was characterized with gradual increase in the pattern of *M(3000)F2$_{KOR}$* with effect from around 19LT through 05LT. Low solar activity (LSA) years have predominantly higher magnitudes than high solar activity (HSA) years for all seasons, thus revealing solar activity dependence of *M(3000)F2$_{KOR}$*. For instance, the highest magnitude were obtained in 1996 (72.0 *sfu*), while the lowest was obtained in 2000 (181.0 *sfu*). Figure 1(b) is the overall seasonal hourly averages of the observations in Figure 1(a). The dashed black arrows depicts the range of magnitude saturation of the *M(3000)F2$_{KOR}$* pattern during each of the seasons. Evidently, the magnitude saturates for about 6 hours (11LT -17LT) for the entire seasons except in June solstice that is short lived. The blue arrow points towards the sharp drop in the *M(3000)F2$_{KOR}$* pattern immediately after sunset, and is expected to correspond to the post-sunset peak in hmF2 [Obrou et al., 2003] owning to the inverse relationship between the two parameters. However, this feature from Figure 1(b) is most pronounced in March equinox, followed by December solstice, and then September equinox, but almost missing in June solstice.

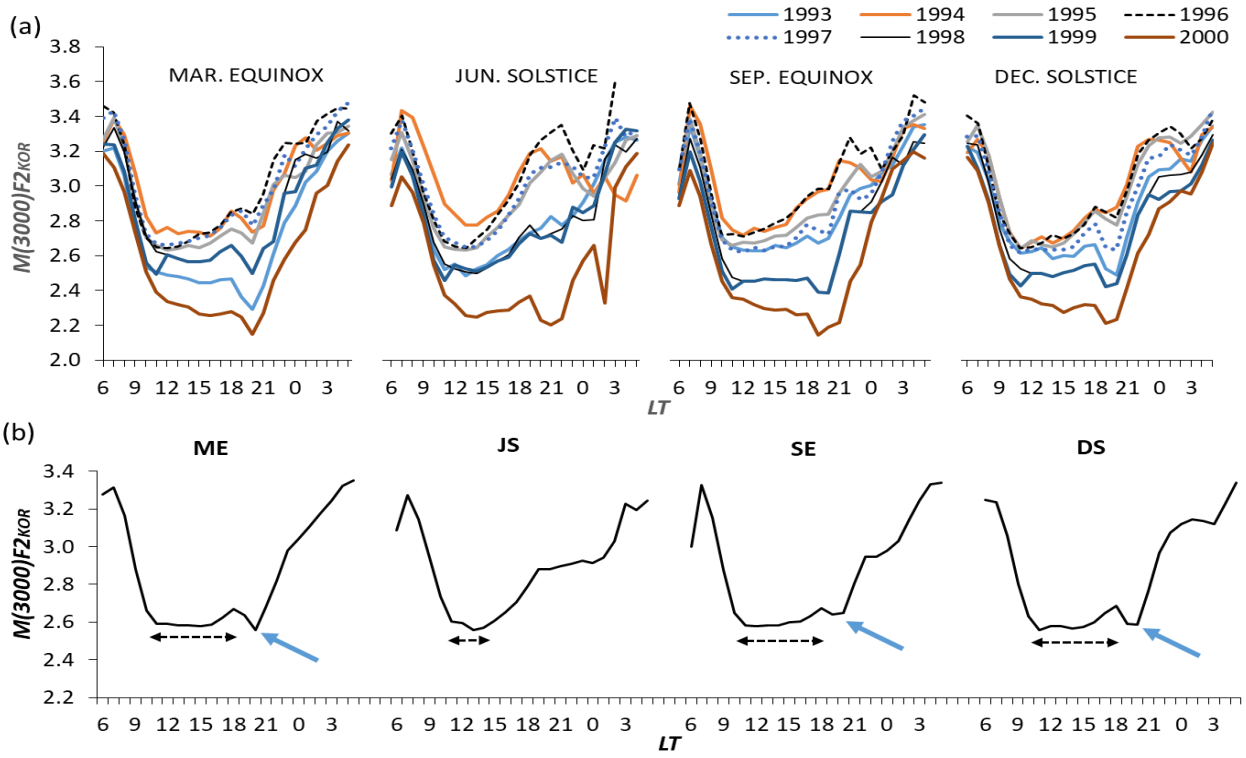

Figure 1: (a) Seasonal hourly pattern of *M(3000)F2* at Korhogo spanning 1993 – 2000, (b) Hourly average variation of the annual year plots in (a). ME is March equinox, JS is June solstice, SE is September equinox, and DS is December solstice.

3.2. Solar activity dependence of M(3000)F2$_{KOR}$.

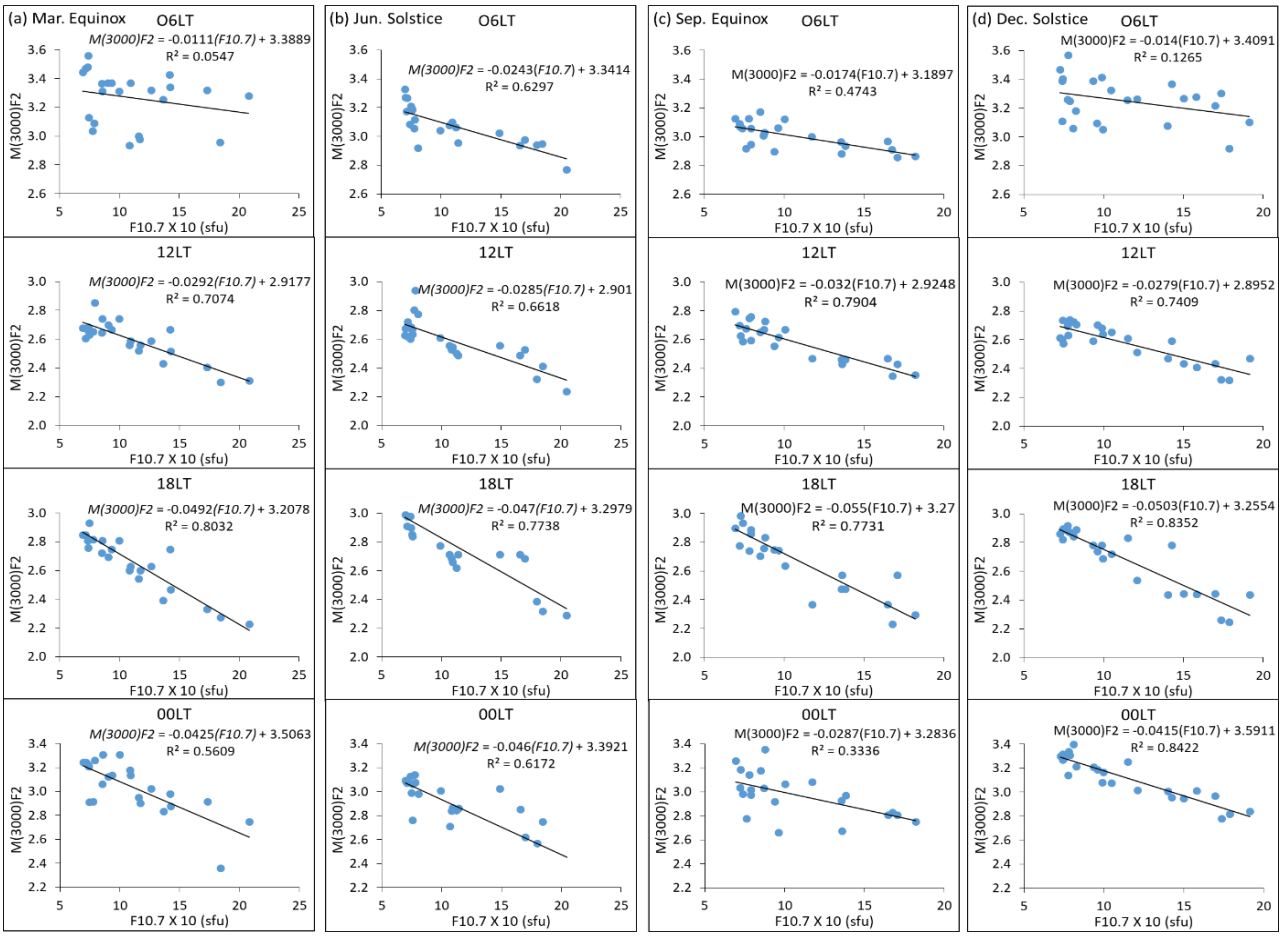

Figure 2: Selected seasonal hourly regression scatter plots of *M(3000)F2$_{KOR}$* versus *F10.7* at 06LT, 12LT, 18LT, and 00LT for (a) March equinox, (b) June solstice, (c) September equinox, and (d) December solstice.

Having established the fact that *M(3000)F2$_{KOR}$* depends on solar activity (as revealed in section 3.1), it is necessary to investigate the extent diurnally and seasonally. Consequently, linear relationship between *M(3000)F2$_{KOR}$* and the solar flux index, *F10.7* was considered, in line with the Regression method technique used by Tukhashvili et al. [2003] such that the diurnal regression coefficient, the slope, and the intercept can be determined. This was achieved by using the monthly averages of *M(3000)F2$_{KOR}$* as the dependent variable and *F10.7* as the independent variable. Figure 2(a-d) highlights some selected regression scatter plots between the two parameters at 06LT, 12LT, 18LT, and 00LT for March equinox, June solstice, September equinox, and December solstice respectively. The scatter plots, in each panel reveals the values of the corresponding regression coefficient (R^2), slope and intercept. The overall presentation for all hours from one season to another is as presented in Table 1. Both Figure 2(a-d) and Table 1 revealed inverse relationship between *M(3000)F2$_{KOR}$* and *F10.7*. R^2 between the two parameters was strong in the solstices when compared with the equinoxes as shown by the bolded values of Table 1. The bolded values represents the highest R^2 magnitude across the seasons per each hour. Apart from few instances/hours when R^2 is low (i.e. < 50%), R^2 ranges from 54-86% and 51-83% during the equinoxes and solstices respectively. The R^2 had average percentage values of 70%, 71%, 75%, and 70% at daytime (06 – 18LT) for March equinox, June solstice, September equinox, and December solstice. At nighttime (18 – 05LT), average regression values are 63%, 54%, 52%, and 73% in similar order of seasons. To further analyse the *M(3000)F2$_{KOR}$* versus *F10.7* relationship, a

graphical representation of Table 1 was presented in Figure 3. The figure revealed similar and coherent pattern in the plots of R^2, the slope, and the intercept at daytime (06 -18LT) during all seasons, but became fragmented and scattered with the nighttime observation. The following were also observed from the figure:

i. a hump in the pattern of R^2 from 06LT to 07LT, followed by a sharp drop at 09LT and then a rise at 10LT across all seasons,
ii. the highest regression magnitude was immediately after sunrise at 07LT, ranging between 77% and 84% across the entire four seasons,
iii. the seasonal dependence of $M(3000)F2_{KOR}$ on $F10.7$ is more pronounced at nighttime in comparison to daytime observations,
iv. a daytime progressive downward excursion in the pattern of the slope up till around 19LT across all seasons, and thereafter an upward excursion through the nighttime period,
v. Seasonal differences are observed in the slope pattern of the $M(3000)F2_{KOR}$ versus $F10.7$ relationship in June solstice and September equinox, especially at nighttime,
vi. an upward jerk in the pattern of the intercept from 06LT to 07LT, followed by an hyperbolic characteristics lasting till around 18LT across all seasons

Table 1: Diurnal variation of the regression coefficient, slope, and intercept for the plots of $M(3000)F2_{KOR}$ versus $F10.7$ for (a) March equinox (ME), (b) June solstice (JS), (c) September equinox (SE), and (d) December solstice (DS).

LT	**R^2**				**Slope**				**Intercept**			
(hour)	ME	JS	SE	DS	ME	JS	SE	DS	ME	JS	SE	DS
6	0.054	**0.629**	0.474	0.126	-0.0011	-0.0024	-0.0017	-0.0014	3.388	3.341	3.189	3.409
7	**0.866**	0.835	0.829	0.767	-0.0028	-0.0027	-0.0029	-0.0026	3.617	3.567	3.651	3.533
8	**0.762**	0.621	0.720	0.606	-0.0026	-0.0024	-0.0028	-0.0026	3.455	3.402	3.461	3.354
9	0.397	0.504	**0.554**	0.531	-0.0022	-0.0022	-0.0024	-0.0025	3.136	3.188	3.148	3.086
10	0.543	0.556	0.751	**0.827**	-0.0024	-0.0029	-0.0027	-0.0026	2.931	3.053	2.943	2.935
11	0.825	0.674	**0.840**	0.790	-0.0027	-0.0032	-0.0034	-0.0026	2.896	2.956	2.954	2.860
12	0.707	0.661	**0.790**	0.740	-0.0029	-0.0028	-0.0032	-0.0027	2.917	2.901	2.924	2.895
13	**0.799**	0.720	0.790	0.732	-0.0030	-0.0030	-0.0035	-0.0030	2.915	2.884	2.965	2.920
14	0.785	0.793	0.770	**0.800**	-0.0033	-0.0032	-0.0035	-0.0031	2.953	2.921	2.971	2.927
15	**0.832**	0.786	0.808	0.740	-0.0038	-0.0034	-0.0039	-0.0034	2.998	2.979	3.027	2.962
16	**0.849**	0.813	0.844	0.767	-0.0039	-0.0038	-0.0040	-0.0036	3.011	3.066	3.045	3.012
17	0.820	**0.828**	0.814	0.789	-0.0043	-0.0044	-0.0049	-0.0042	3.094	3.187	3.164	3.133
18	0.803	0.773	0.773	**0.835**	-0.0049	-0.0047	-0.0055	-0.0050	3.207	3.297	3.270	3.255
19	0.778	0.775	0.657	**0.805**	-0.0054	-0.0054	-0.0068	-0.0057	3.225	3.470	3.380	3.248
20	0.753	**0.820**	0.718	0.723	-0.0057	-0.0070	-0.0066	-0.0051	3.176	3.630	3.372	3.177
21	0.696	**0.822**	0.751	0.765	-0.0051	-0.0071	-0.0069	-0.0050	3.231	3.667	3.568	3.337
22	0.388	**0.793**	0.576	0.708	-0.0045	-0.0071	-0.0050	-0.0049	3.286	3.681	3.497	3.524
23	0.662	0.689	0.536	**0.801**	-0.0048	-0.0052	-0.0044	-0.0048	3.501	3.476	3.430	3.630
0	0.560	0.617	0.333	**0.842**	-0.0042	-0.0046	-0.0028	-0.0041	3.506	3.392	3.283	3.591
1	0.545	0.521	0.232	**0.816**	-0.0038	-0.0044	-0.0017	-0.0038	3.537	3.380	3.214	3.583
2	**0.832**	0.494	0.197	0.776	-0.0029	-0.0048	-0.0019	-0.0030	3.489	3.523	3.355	3.478
3	**0.599**	0.103	0.417	0.543	-0.0026	-0.0019	-0.0024	-0.0023	3.528	3.421	3.506	3.380
4	0.606	0.013	0.535	**0.607**	-0.0020	-0.0005	-0.0022	-0.0022	3.540	3.112	3.568	3.483
5	0.351	0.002	0.552	**0.560**	-0.0012	-0.0011	-0.0020	-0.0016	3.487	3.220	3.553	3.523

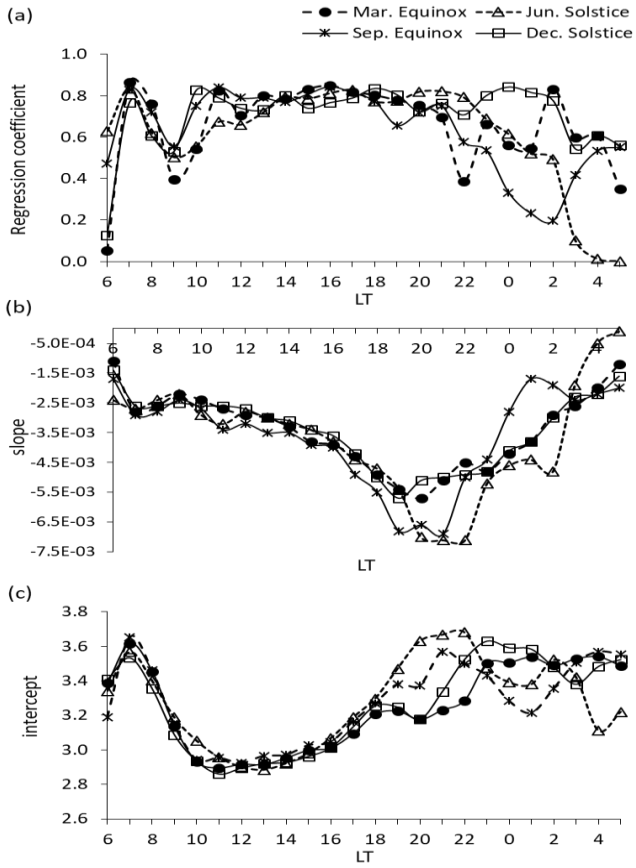

Figure 3: Average diurnal pattern of (a) the regression coefficient, (b) slope of equation, and (c) intercept of equation for the entire 1993 – 2000 binned into various seasons.

3.3. Obtaining the M(3000)F2$_{KOR.}$ Constructed Model [M(3000)F2$_{CM}$]

The associated diurnal equations obtained for all seasons in the linear regression plot of the *M(3000)F2$_{KOR}$* versus *F10.7* relationship (Figure 2 and Table1) were used to obtained an empirical constructed model equation for the equatorial latitude in the African sector *(M(3000)F2$_{CM}$)*, and is given by the expression in equation (3).

$$M(3000)F2_{CM}(m)_i = a_i(m) * (F10.7) + b_i \qquad (3)$$

where 'a_i' is the slope of regression between *M(3000)F2$_{KOR}$* and *F10.7*, 'b_i' is the intercept, 'm' the seasonal factor, and 'i' is the diurnal factor. *F10.7* is the monthly average solar irradiance flux index at the wavelength of 10.7cm, a proxy for solar activity levels. 'a_i', 'b_i', and 'm' values are as presented in Table 1. Further, the values for *M(3000)F2$_{CM}$* - that is the *M(3000)F2* constructed model were predicted for various seasons at low-, moderate-, and high-solar activities (i.e. LSA, MSA, HSA). This was achieved by writing a MATLAB code that takes care of the diurnal and seasonal factors in terms of the slope and the intercept. Solar activity condition was accommodated by setting *F10.7* to be 70 sfu, 120 sfu, and 250 sfu for LSA, MSA, and HSA conditions respectively.

Figure 4 highlights the variations of the obtained model *(M(3000)F2$_{CM}$)* for the entire seasons at LSA (*F10.7 = 70sfu*), MSA (*F10.7 = 120sfu*), and HSA (*F10.7 = 250sfu*) conditions. Close and similar features of *M(3000)F2$_{CM}$* were seen during the entire seasons at daytime (06-18LT) irrespective of solar activity conditions. At all levels of solar activity, seasonal variations are well captured at nighttime immediately after sunset. The model revealed the exact features of the ionospheric propagation factor in the equatorial region. Large trough/crests at

daytime/nighttime are observable. Generally, HSA presents the minimum trough magnitudes of about 1.84 while LSA presents the maximum trough magnitude of 2.71, revealing the solar activity dependence of the propagation factor. A striking feature in the result is the sharp drop in $M(3000)F2_{CM}$ after sunset (which is expected to correspond to the post-sunset peak in hmF2). The evening-time drop in $M(3000)F2_{CM}$ after sunset (at 20LT) is well developed in all seasons of the HSA condition. For the LSA and MSA conditions, the feature was also observable at 20LT in all seasons, except for June solstice of the low solar activity where the feature is not well pronounced at 20LT but instead extended to around 23LT before manifesting. In all, the $M(3000)F2_{CM}$ had been observed to be better than the $M(3000)F2_{KOR}$ (i.e. June solstice observation in Figure 1b).

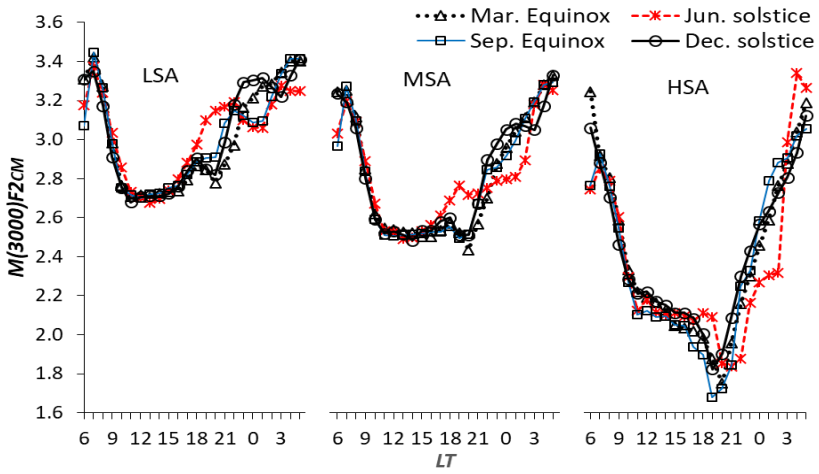

Figure 4: Values obtained for $M(3000)F2_{CM}$ for all seasons at LSA (*F10.7 = 70sfu*), MSA (*F10.7 = 120sfu*), and HSA (*F10.7 = 250sfu*).

The original Shimazaki (1955) relation relating *hmF2* and *M(3000)F2* together is of the form:

$$h_mF2 = \frac{1490}{M(3000)F2} - 176 \qquad (4)$$

However, Bradley and Dudeney (1973) proposed higher step forward, such that the *M(3000)F2* in equation (4) is replaced by [*M(3000)F2* + ΔM], the correction term; which depends on the $\frac{foF2}{foE}$ ratio.

This is such that

$$\Delta M = 0.18/(X - 1.4) \qquad (5)$$

where X = $\frac{foF2}{foE}$

However, Eyfrig (1972) had suggested another equation taking into account the solar cycle Zurich Sunspot Number (*R*), and given by:

$$\Delta M = 0.18/(X - 1.4) + 0.096 * (R - 25)/150 \qquad (6)$$

Bilitza et al. (1979) later proposed a formula beyond equations (4) and (6), now taking into account the parameter R, and the geomagnetic latitude given by:

$$\Delta M = (F1(R) * F4(R, lat))/(\frac{foF2}{foE} - F2(R)) + F3(R) \qquad (7)$$

where

$F1 = 2.32E - 3 * R + 0.222,$

$$F2 = 1.2 - 1.16E-2 * \exp(2.39E-2 * R),$$
$$F3 = 0.096 * (R - 25)/150,$$
$$F4 = 1 - \left(\frac{R}{150}\right) * \exp\left(-\frac{lat^2}{1600}\right)$$

Equation (7) was eventually introduced into the IRI map for obtaining *hmF2* from *M(3000)F2* (e.g. Rawer and Eyfrig, 2004).

We therefore write our generated expression for the *hmF2* in the equatorial region (following Shimazaki expression) as

$$hmF2 = \frac{1490}{M(3000)F2_{CM}(m)_i} - 176 \quad (8)$$

Substituting for $M(3000)F2_{CM}$ in equation (3),

$$hmF2 = \frac{1490}{a_i(m) * (F10.7) + b_i} - 176 \quad (9)$$

Here, 'a_i' is the slope of regression between *M(3000)F2* and *F10.7*, 'b_i' is the intercept, 'm' the seasonal factor, and 'i' is the diurnal factor. *F10.7* is the monthly average solar irradiance flux index. Equation (9) may therefore be integrated into the African regional model in the equatorial latitude, and more importantly into the IRI-(ITU-R) model.

3.4. Validating the Constructed Model ($M(3000)F2_{CM}$) with Ouagadougou M(3000)F2 data

Figure 5 presents the diurnal variation between *M(3000)F2* obtained at Ouagadougou ($M(3000)F2_{OUA}$) and $M(3000)F2_{CM}$ during (a) high solar activity year 1991; and (b) low solar activity year 1995 for selected months representing different seasons. The clustered bar chart at the background depicts the percentage deviation between the two. In this sense, a downward trend (or flow) in the background bar chart presentation indicates overestimation of the $M(3000)F2_{OUA}$ by the $M(3000)F2_{CM}$; and an upward trend indicates over estimation of $M(3000)F2_{OUA}$ by $M(3000)F2_{CM}$; The percentage deviation is given by:

$$\%\, Deviation = \frac{M(3000)F2_{OUA} - M(3000)F2_{CM}}{M(3000)F2_{OUA}} \quad (10a)$$

For both years (1991 and 1995), monthly average values of *M(3000)F2* for the selected months (January, April, July, and October representing December solstice, March equinox, June solstice, and September equinox respectively) at Ouagadougou were directly used based on the methodology in section 2. However, for the $M(3000)F2_{CM}$ computation, the diurnal values obtained for the slope and intercept (depicted in Table 1) during each season was used together with *F10.7* magnitude of *208.1 sfu* for 1991 and *77.2 sfu* for 1995. The following observations were noted from the figure:

i. the model [$M(3000)F2_{CM}$] correctly predict the general diurnal structure of the observed *M(3000)F2* obtained at Ouagadougou [$M(3000)F2_{OUA}$];
ii. for both the HSA year 1991 (Fig. 5a) and the LSA year 1995 (Fig. 5b), the percentage deviation of the model in comparison with the observed $M(3000)F2_{OUA}$ is depletion (indicating over-estimation) during the solstices [Fig. 5a – (i, iii); 5b (i, iii)], and enhancement (under-estimation) during the equinoxes [Figure 5a – (ii, iv); 5b (ii, iv)].

iii. the RMS_{dev} magnitude between the two parameters are 0.0053, 0.0202, 0.0043, and 0.0173 for the months representing March equinox, June solstice, September equinox, and December solstice respectively for HSA year (1991); and 0.0533, 0.0469, 0.0385, and 0.0200 in similar order of seasons during the LSA (1995) period, indicating better representation of the observed $M(3000)F2_{OUA}$ by the constructed model during HSA period in comparison to LSA period.

iv. the average magnitude of the RMS_{dev} revealed better agreement during equinoxes than solstices for both conditions of solar activity;

v. the diurnal post-sunset trough in $M(3000)F2_{OUA}$ around 20LT, which is one of the major features of *M(3000)F2* at equatorial region is well captured by the empirical constructed model developed during the entire seasons;

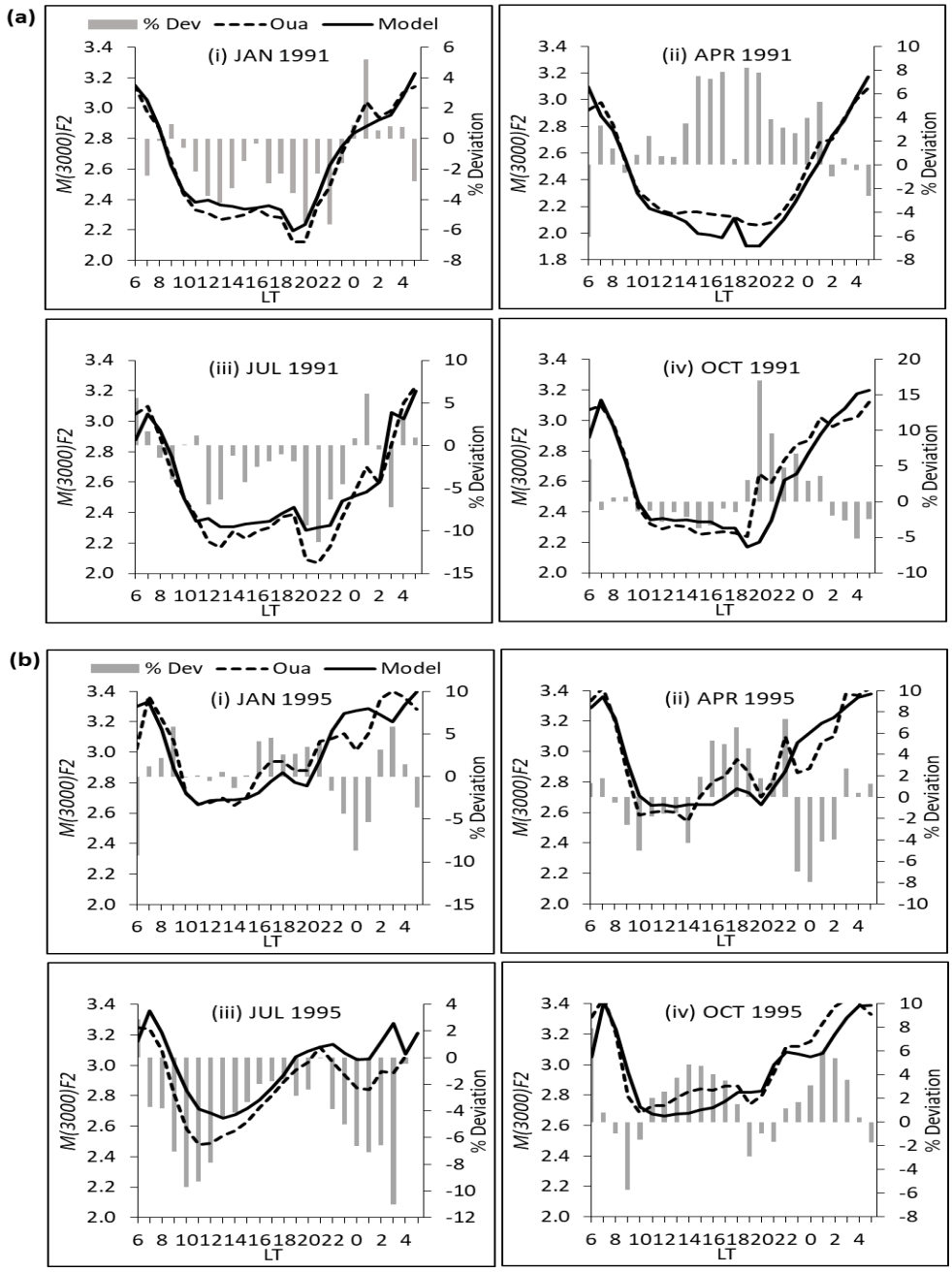

Figure 5: Diurnal variation between *M(3000)F2* obtained at Ouagadougou ($M(3000)F2_{OUA}$) and $M(3000)F2_{CM}$ during (a) high solar activity year (1991) and (b) low solar activity (1995) for selected months representing different seasons. The clustered bar chart at the background depicts the percentage variation between the two.

3.5. Comparison of the IRI-2012 M(3000)F2 data [$M(3000)F2_{IRI}$] with Ouagadougou M(3000)F2 data

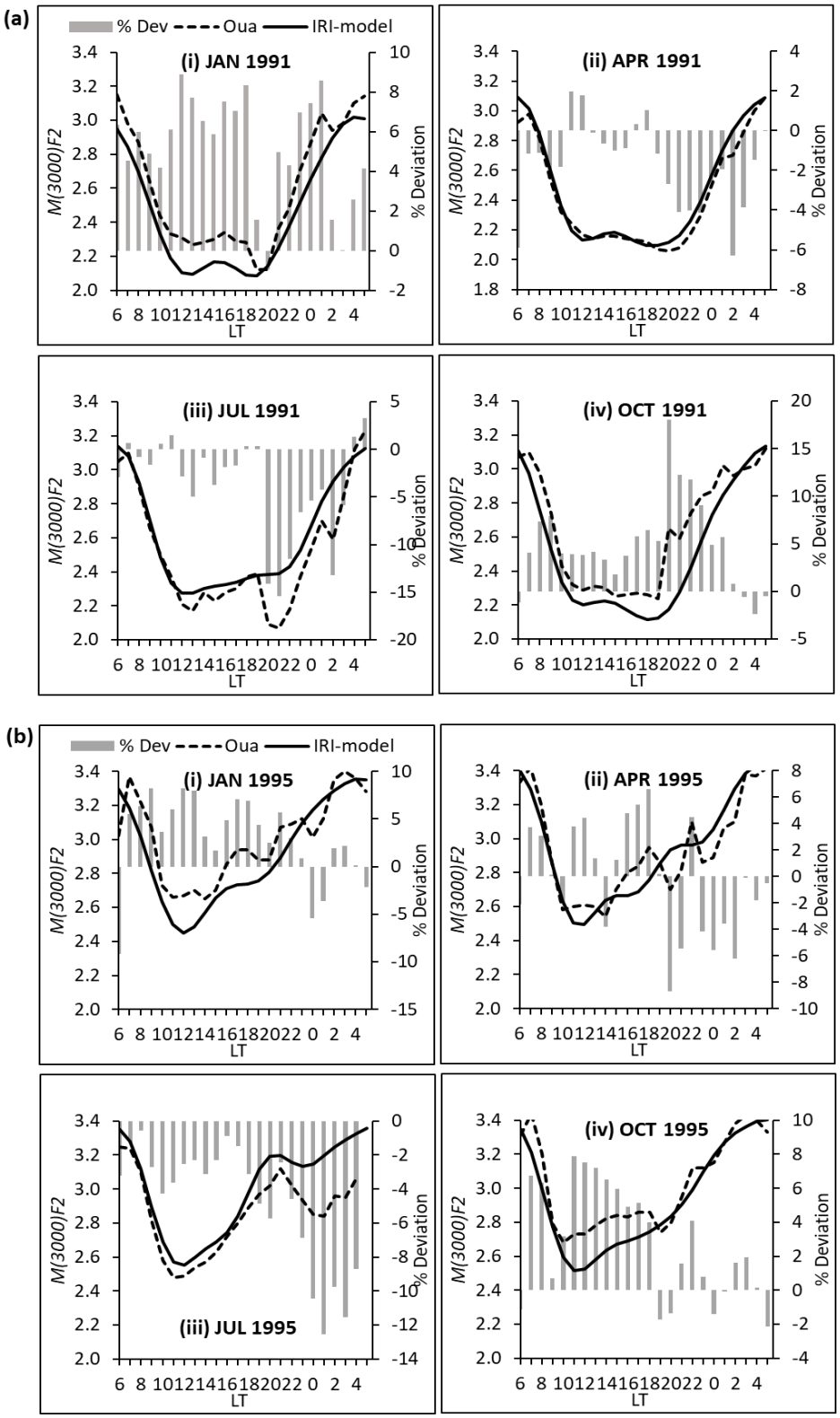

Figure 6: Diurnal variation between *M(3000)F2* obtained at Ouagadougou ($M(3000)F2_{OUA}$) and IRI-2016 (ITU-R) predicted model [$M(3000)F2_{IRI}$] during (a) high solar activity year (1991) and (b) low solar activity (1995) for selected months representing different seasons. The clustered bar chart at the background depicts the percentage variation between the two.

The deviation plot between the observed value at Ouagadougou ($M(3000)F2_{OUA}$) and that of the IRI ($M(3000)F2_{IRI}$) are highlighted in Figure 6, yet again for the high- (Fig. 6a) and low-solar (Fig. 6b) activity years The clustered bar chart at the background depicts the percentage variation between the two.
Here,

$$\%\ Deviation = \frac{M(3000)F2_{OUA} - M(3000)F2_{IRI}}{M(3000)F2_{OUA}} \qquad (10b)$$

The variation during HSA period (Fig. 6a) revealed an under-estimation of $M(3000)F2_{OUA}$ by the IRI observation for months representing December solstice (Fig. 6a(i)) and September equinox (Fig. 6a(iv)). Similar over-estimation pattern was observed also for both the December solstice and September equinox months during the LSA period (Figs. 6b (i, iv). For the other months representing March equinox (Figs. 6a (ii), 6b (ii)) and June solstice (Figs. 6a (iii), 6b (iii)) $M(3000)F2_{OUA}$ is overestimated by $M(3000)F2_{IRI}$ for both the HSA and LSA periods.

Table 2: (a) Seasonal Root Mean Square deviation values for the $M(3000)F2_{OUA}$ versus $M(3000)F2_{CM}$ and $M(3000)F2_{OUA}$ versus $M(3000)F2_{IRI}$ pairs during HSA and LSA periods for the months depicting various seasons at daytime hours, nighttime hours, and the entire 24 hours. The bolded values with suffix 'a' represent the better performed pair at each category of local time for High solar activity; while the bolded values with suffix 'b' presents same under low solar activity condition. (b) Annual average of Root Mean Square deviation values at daytime, nighttime and entire 24-hours observation yet for the pairs under consideration.

	Month (Season)	**Local Time (LT) coverage**	**HSA**		**LSA**	
			$M(3000)F2_{OUA}$ vs. $M(3000)F2_{CM}$	$M(3000)F2_{OUA}$ vs. $M(3000)F2_{IRI}$	$M(3000)F2_{OUA}$ vs. $M(3000)F2_{CM}$	$M(3000)F2_{OUA}$ vs. $M(3000)F2_{IRI}$
(a)	**Jan. (Dec. solstice)**	Daytime	**0.055[a]**	0.159	**0.112[b]**	0.187
		Nighttime	**0.082[a]**	0.140	**0.114[b]**	0.136
		Entire 24 hr.	**0.099[a]**	0.212	**0.176[b]**	0.219
	Apr. (Mar. equinox)	Daytime	0.105	**0.059[a]**	**0.087[b]**	0.096
		Nighttime	0.095	**0.081[a]**	0.143	**0.138[b]**
		Entire 24 hr.	0.141	**0.100[a]**	**0.167[b]**	0.168
	Jul. (Jun. solstice)	Daytime	0.092	**0.057[a]**	0.149	**0.070[b]**
		Nighttime	**0.132[a]**	0.197	**0.939[b]**	0.995
		Entire 24 hr.	**0.161[a]**	0.205	**0.951[b]**	0.997
	Oct. (Sept. equinox)	Daytime	**0.070[a]**	0.122	**0.121[b]**	0.167
		Nighttime	**0.179[a]**	0.221	0.098	**0.065[b]**
		Entire 24 hr.	**0.192[a]**	0.253	**0.156[b]**	0.179
(b)	**Entire year**	Daytime	**0.081[a]**	0.099	**0.117[b]**	0.130
		Nighttime	**0.122[a]**	0.160	**0.324[b]**	0.334
		Entire 24 hr.	**0.148[a]**	0.193	**0.363[b]**	0.391

The magnitudes of the root mean square deviation for both the $M(3000)F2_{OUA}$ versus $M(3000)F2_{CM}$ and $M(3000)F2_{OUA}$ versus $M(3000)F2_{IRI}$ pairs during HSA and LSA conditions for the months depicting various seasons at daytime hours, nighttime hours, and the entire 24 hours are presented in Table 2. The bolded values with suffix 'a' represent the better performed pair (the lower the value the better the relationship between the two) at each

category of local time for High solar activity; while the bolded values with suffix 'b' presents same under low solar activity condition. Generally for both the HSA and LSA conditions from Table 2a, the $M(3000)F2_{OUA}$ versus $M(3000)F2_{CM}$ pair recorded better relationship than the $M(3000)F2_{OUA}$ versus $M(3000)F2_{IRI}$ pair except for the April (March equinox) observation of the HSA period. The seasonal observation in Table 2a is further buttressed in Table 3, revealing the frequency of best relationship/performance for the $M(3000)F2_{OUA}$ versus $M(3000)F2_{CM}$ and $M(3000)F2_{OUA}$ versus $M(3000)F2_{IRI}$ pairs during HSA and LSA conditions at daytime hours, nighttime hours, and the entire 24 hours. One observed here that while there are variations in the frequency distribution in the performance of both the $M(3000)F2_{OUA}$ versus $M(3000)F2_{CM}$ and $M(3000)F2_{OUA}$ versus $M(3000)F2_{IRI}$ pairs at daytime and nighttime hours, the entire 24 hours observation summarizes the whole process in which a better relationship exists between the $M(3000)F2_{OUA}$ versus $M(3000)F2_{CM}$ pair over that of the $M(3000)F2_{OUA}$ versus $M(3000)F2_{IRI}$ pair in the percentage ratio of 75% : 25% for HSA condition and 100% : 0% for the LSA condition.

Table 3: Frequency of best performance for the $M(3000)F2_{OUA}$ versus $M(3000)F2_{CM}$ and $M(3000)F2_{OUA}$ versus $M(3000)F2_{IRI}$ pairs during HSA and LSA conditions at daytime hours, nighttime hours, and the entire 24 hours.

Period	**HSA**		**LSA**	
	$M(3000)F2_{OUA}$ vs. $M(3000)F2_{CM}$	$M(3000)F2_{OUA}$ vs. $M(3000)F2_{IRI}$	$M(3000)F2_{OUA}$ vs. $M(3000)F2_{CM}$	$M(3000)F2_{OUA}$ vs. $M(3000)F2_{IRI}$
Daytime	2	2	3	1
Nighttime	3	1	2	2
Entire 24 hr.	3	1	4	0

From the annual average presentation of the root-mean-square deviation in Table 2b, the following were noted:

a. The constructed model $M(3000)F2_{CM}$ presents better morphology/pattern of the observed $M(3000)F2_{OUA}$ than the $M(3000)F2_{IRI}$ during the daytime, nighttime, and entire 24-hours irrespective of the solar activity condition (i.e. 0.081 < 0.009, 0.122 < 0.160, 0.148 < 0.193 for HSA and 0.117 < 0.130, 0.324 < 0.334, 0.363 <0.391 for LSA);
b. There is better agreement/relationship in the $M(3000)F2_{OUA}$ versus $M(3000)F2_{CM}$ during HSA than LSA condition (i.e. 0.081 < 0.117, 0.112 < 0.324, 0.148 < 0.363) irrespective of whether it is daytime, nighttime, or entire 24-hour observation;
c. The $M(3000)F2_{IRI}$ performed better with the $M(3000)F2_{OUA}$ during HSA than LSA condition (i.e. 0.099 < 0.130, 0.160 < 0.334, 0.193 < 0.391) irrespective of whether it is daytime, nighttime, or entire 24-hour observation;
d. A better relationship exists in the $M(3000)F2_{OUA}$ versus $M(3000)F2_{CM}$ and $M(3000)F2_{OUA}$ versus $M(3000)F2_{IRI}$ during the daytime than at nighttime irrespective of solar activity condition.

Conclusion

An empirical $M(3000)F2_{CM}$ model has been constructed for an equatorial station in the African sector. This model is uniquely dependent on solar flux, F10.7 (proxy). The model allows the prediction of diurnal, seasonal and solar cycle variation of the *M(3000)F2* parameter. The raw daily hourly values of $M(3000)F2_{KOR}$ measured using the Ionospheric Prediction Service (IPS-42) sounder located at Korhogo Ionospheric Observatory(Latitude $+9.3^0$, Longitude -5.4^0, dip Latitude -0.67^0) were used for the study. The extracted $M(3000)F2_{KOR}$ data were used to compute the monthly hourly average values of $M(3000)F2_{KOR}$. The entire 24 hours, eight years' worth of data, spanning 1993-2000, for magnetically quiet conditions (Ap < 26) were used. It was established among others that the *M(3000)F2* is inversely proportional to the *F10.7* for all seasons. The constructed $M(3000)F2_{CM}$ model performed well when tested at different solar flux conditions. The general performance of the empirical constructed *M(3000)F2* model is validated with observed data from Ouagadougou (Geographic latitude 12.4^0N, longitude

358.5^0, dip Latitude 5.7^0) and performed better in comparison with that of the IRI-model at some instances. Both the $M(3000)F2_{CM}$ and $M(3000)F2_{IRI}$ performed better with the observed $M(3000)F2_{OUA}$ during high solar activity in comparison with the low solar condition irrespective of the local time period.

While the two recent *hmF2* IRI-2016 model options - Altadill-Magdaleno-Torta-Blanch [AMTB2013 – Altadil et al., 2013] and SHUbin [SHU-2015 – Shubin et al., 2013; Shubin, 2015] were developed from a very large dataset of observed *hmF2* values from ground-based and satellite observations, the third option, Bilitza-Sheikh-Eyfrig (BSE-1979 – Bilitza et al., 1979), added to the IRI-2016 option, and which forms the basis for the *hmF2* model in IRI-2012 was inferred from the CCIR *M(3000)F2* maps from a global representations of close to 152 ionosondes (Bilitza et al., 1979). Adeniyi et al. [2021] observed that each of this three-options display varying strengths and shortcomings depending on the local time, season, solar activity period, and latitude. It therefore follows that the approach of obtaining *hmF2* from *M(3000)F2* should be improved upon and not dropped entirely, by employing larger database spanning different latitudes and solar activity conditions; since even both the AMTB2013 and SHU-2015 have their challenges as well. It is worth mentioning that the results obtained in this work suggest that the new constructed model has a measure of potential for its use in the equatorial region.

Acknowledgement

The Authors would like to appreciate the Natural Resources Canada group for making available the solar flux *F10.7* data at http://www.spaceweather.ca/solarflux/sx-5-en.php. The IRI-2012 *M(3000)F2* model data was obtained from https://ccmc.gsfc.nasa.gov/modelweb/models/iri2012_vitmo.php. Both the Korhogo and Ouagadougou data used in this work can be accessed through http://eprints.lmu.edu.ng/2918/.

References

Adebesin, B. O., J. O. Adeniyi, I. A. Adimula, S. J. Adebiyi, S. O. Ikubanni, O. A. Oladipo, and A. O. Olawepo (2019): Pattern of Ionization Gradient, Solar Quiet magnetic element, and F2-layer bottomside thickness parameter at African equatorial location. ***Radio Science***. **54.** 415-425, doi:10.1029/2018 RS006742.

Adebesin, B.O., A. B. Rabiu, O. S. Bolaji, J. O. Adeniyi, and C. Amory-Mazaudier (2018a): Ionospheric Climatology at Africa EIA trough stations during Descending Phase of Sunspot Cycle 22. ***Journal of Atmos. and Solar-Terrestrial Physics***. **172,** 83-99, doi: 10.1016/j.jastp. 2018.03.009. *https://doi.org/10.1016/*j.jastp.2018.03.009.

Adebesin, B.O., A. B. Rabiu, O. K. Obrou, and J. O. Adeniyi (2018b): Ionospheric peak electron density and performance evaluation of IRI-CCIR near magnetic equator in Africa during two extreme solar activities. *Space Weather*. 16(3) 230-244, doi:10.1002/2017SW001729.

Adebesin, B.O., and J. O. Adeniyi (2018): F2-layer height of the Peak Electron Density (hmF2) dataset in inferring Vertical Plasma Drift: Data of Best Fit. ***Data in Brief***. **19**, 59-66. doi:10.1016/j.dib.2018.04.141.

Adebiyi, S.J., Adeniyi, J.O., Adebesin, B.O., Ikubanni, S.O., Adimula, I.A., Oladipo, O.A., Olawepo, A.O., Adekoya, B.J., and Joshua, B.W. (2020): Comparative investigation of the digisonde derived electron density and IRI profiles at a station near the African magnetic equator during low solar activity. *Journal of Geophysical Research – Space Physics.* **125(3).** doi:10.1029/ 2019JA027477.

Adeniyi, J.O., Adebesin, B.O., Ikubanni, S.O., Adebiyi, S.J., Adekoya, B.J., and Babatunde, J. (2021): Validating IRI-2016 for quiet-time F2-region peak electron density height (hmF2) at different latitudes during moderate solar activity. ***Advances in Space Research.*** *(Article in press)* https://doi.org/10.1016/j.asr.2021.04.025.

Adeniyi, J.O, Olawepo, A.O and Obrou, O.A. (2010): Response of the African equatorial ionosphere to the Jan 13-15, 1999 magnetic storm. Centrepoint (Science Edition). 16. No.7-14.

Adeniyi, J. O, Bilitza, D., Radicella, S. M and Willougby, A. A. (2003): Equatorial F2-peak parameter in the IRI model. Adv. Space Res. 31(3), 507 – 512. doi: 10.1016/s0273-1177(03)00039s-5.

Altadill, D., Magdaleno, S., Torta, J.M., Blanch, E., 2013. Global empirical models of the density peak height and of the equivalent scale height for quiet conditions. Adv. Space Res., 52, 1756– 1769, doi:10.1016/j.asr.2012.11.018

Bilitza D, Mckinnell L.A., Reinisch B.W. and Fuller-Rowell, T. (2011): International reference ionosphere today and in future. J. Geod, 85:909-920, doi:10.1007/s00190-010-0427-x

Bilitza, D., Sheikh, N. M., and Eyfrig, R. (1979): A global model for the height of the F2-peak using M3000 values from CCIR, Telecommunication Journal, 46, 549–553.

Bradley, P. A. and Dudeney, J. R. (1973): A simple model of the vertical distribution of electron concentration in the ionosphere, J. Atmos. Terr. Phys., 35, 2131–2146.

Ehinlafa, O.E, Falaiye, O.A and Adeniyi, J.O. (2010): Comparison of observed hmF2 and IRI 2007 model with M(3000)F2 estimation of hmF2 at low solar activity for an equatorial station. Adv. Space Res. 46(1),89-93, doi: 10/1016/j.asr.2010.02.018

Eyfrig, R. (1972): Zur Korrektur der Shimazaki-Formal, Kleinheubacher Berichte. 16, 227-231

Falayi E.O., Adebesin, B. O, Bolaji, O.S. (2018): The Impact of Coronal mass ejection on the horizontal geomagnetic fields and the induced Geoelectric fields. ***Advances in Space Research*. 61**, 985 – 1003. doi:10.1016/j.asr.2017 .11.005.

Hoque, M.M. and N. Jakowski (2012): A new global model for the ionospheric F2 peak height for radio wave propagation. Ann. Geophys., **30**, 797–809.

Liu, C., Zhang,. M.L., Wan, W., Liu, L. and Ning, B. (2008): Modeling M(3000)F2 based on empirical orthogonal analysis method. Radio Sci. 43, RS1003, doi:10.1029/2007RS003694

Liu, L., Luan, X., Wan, W., Lei, J., Ning, B., 2003. Seasonal behavior of equivalent winds over Wuhan derived from ionospheric data in 2000–2001. ***Adv. Space Res***. 32 (9), 1765–1770, doi:10.1016/S0273-1177(03)90474-1

Obrou, O.K., Bilitza, D., Adeniyi, J.O., Radicella, S.M. (2003) Equatorial F2- layer peak height and correlation with vertical ion drift and M(3000)F2. ***Advances in Space Research***. **31**, 513–520.

Oyekola, O.S. (2010): Variation in the ionospheric propagating factor, M(3000)F2. ***Adv Space Res***. 46(1), 74-80.

Oyeyemi E.O., McKinnell L. A. and Poole A.W.V. (2007): Neural network based prediction techniques for global modeling of M(3000)F2 ionospheric parameter. ***Adv Space Res*** 39(5):643–650. doi:1016/j.asr.2006.09.038

Rawer, K. and R. Eyfrig (2004): Improving the M(3000)-hmF2 relation. Advances in Space Research, 878-879

Tukhashvili, k, Kandashvili, V and Mdinaradze, J.O. (2003): On modelling of the diurnal variation of the coefficient of computation of tilt sounding from vertical sounding of ionosphere. Georgians Electronic Scientific Journals. 46-58

Shimazaki, T.: World daily variability in the height of the maximum electron density of the ionospheric F2-layer, (1955): ***J. Radio Res. Lab.,* 2**, 85–97.

Shubin, V.N., 2015. Global median model of the F2-layer peak height based on ionospheric radio-occultation and ground-based digisonde observations. ***Adv. Space Res.,*** 56, 916–928, doi:10.1016/j.asr.2015.05.029.

Shubin, V.N., Karpachev, A.T., Tsybulya, K.G., 2013. Global model of the F2 layer peak height for low solar activity based on GPS radio occultation data. J. Atmos. Sol. Terr. Phys., 104, 106–115, doi:10.1016/j.jastp.2013.08.024.

Zhang, M.L, Chunxu, L, Weixing W, Libo L and Baiqi N. (2010): Evaluation of global modeling of M(3000)F2 and hmF2 based on alternative empirical orthogonal function expansions. ***Adv. Space Res***. 46.1024-1031, doi:10/1016/J.asr.2010. 06.004